Oxygen Reduction Reaction Catalyzed by Metal-Nitrogen-Carbon Hybrids Derived from Metal-Organic Frameworks: Optimized Performance by Zinc Porogen

John Diniz,[a] Eaindar Soe,[a] Jia En Lu,[a] Jesse Hauser,[a] Ahmad Shaabani,[b] Scott R. J. Oliver [a,*], Shaowei Chen [a,*]

[a] Department of Chemistry and Biochemistry, University of California, 1156 High Street, Santa Cruz, CA 95064, United States

[b] Department of Chemistry, Shahid Beheshti University, PO Box 19396-4716, Tehran, Iran

* E-mail: soliver@ucsc.edu, shaowei@ucsc.edu

Abstract

Carbon-based catalysts have been attracting extensive attention as viable candidates to replace platinum towards oxygen reduction reaction, a critical process at fuel cell cathode. An advancement has been the development of carbon-supported iron carbide (Fe_3C/C) catalysts derived from the pyrolysis of metal organic frameworks (MOFs). In the present study, a series of Fe_3C/C nanocomposites were prepared by controlled pyrolysis of FeMOF-NH_2 with a systemic variation of the iron and zinc compositions in the MOF precursor. Scanning/transmission electron microscopy, X-ray diffraction, and X-ray photoelectron spectroscopic measurements were carried out to examine the morphologies, structures, and elemental composition of the nanocomposites, while nitrogen adsorption/desorption and Raman studies were used to characterize the surface area and porosity. It was found that an optimal zinc to iron feeding ratio was required to produce a catalyst with a preferential pore size distribution. Electrochemical

measurements revealed that the sample derived from 20% zinc replacement in the FeMOF-NH_2 precursor exhibited the best electrocatalytic activity in alkaline media among the series, with the most positive onset potential and highest limiting current, which coincided with the highest surface area and porosity. The results suggest that deliberate structural engineering is critical in manipulating and optimizing the electrocatalytic activity of metal,nitrogen-codoped carbon nanocomposites.

Introduction

Fuel cells are an important technology in the pursuit of green energy and reduced pollution to the environment, where electricity is generated by oxidation of fuel molecules at the anode and reduction of oxygen at the cathode (Ozoemena, 2016). In polymer electrolyte membrane fuel cells (PEMFC), while the thermodynamics of the oxygen reduction reaction (ORR) is favorable, the poor kinetics necessitate the use of an effective electrocatalyst. Therefore, rational design and engineering of high-performance electrocatalysts for ORR is vital in the advancement of PEMFC technology. In current practice, platinum nanoparticles supported on graphitic carbon (Pt/C) are utilized as the catalyst of choice, but the high cost and scarcity of platinum prevents the technology from being viable. Therefore, catalysts free of precious metals have been attracting particular attention. Within this context, porous carbon doped with select metal and nonmetal elements have been found to exhibit apparent ORR activity, with a performance that even rivals that of Pt/C (Hu et al., 2015, Lu et al., 2019), due to their high surface area, electrical conductivity, and chemical stability (Chen et al., 2014, Peng et al., 2018).

One of the advancements is the development of nanocarbon-supported iron carbide catalysts (Tan et al., 2019, Wang et al., 2018). For instance, a nanocomposite based on iron carbide nanoparticles encapsulated within a hollow carbon sphere (Fe_3C-Fe,N/C) has been

synthesized from melamine and iron(III) chloride using a triblock copolymer as a template and exhibited a high surface area of 879.5 m^2g^{-1} and apparent electrocatalytic activity towards ORR (Tan et al., 2018). Activation in an inert atmosphere of the similar transition metal-polymer composite through pyrolysis can further improve the catalytic activity. Mixtures of low-cost transition metal salts and nitrogen precursors for the macrocycles can also be used to prepare ORR catalysts (Lefevre et al., 2009). Fe_3C/C catalysts have also been derived from the pyrolysis of polymers such as poly(1,8-diaminonaphthalene), polyvinylpyrrolidone, and polyacrylamide (Xiao et al., 2015, Liu et al., 2019, Chen et al., 2019a, Chen et al., 2019b). Fe_3C/C catalysts derived from organic materials coordinating with iron have also shown good ORR activity (Zhang et al., 2019, Hu et al., 2014, Ferrandon et al., 2012). It is believed that iron carbide can affect the work function of carbon leading to favorable oxygen adsorption (Wang et al., 2018).

One effective strategy to prepare such carbon-based ORR catalysts is controlled pyrolysis of metal-organic frameworks (MOFs), where metal and nonmetal elements from the MOF precursors are doped into the carbon skeletons (Li et al., 2019). Thus, a catalyst can be designed from the bottom up to take advantage of the ready manipulation of the MOF composition and structure. The first MOF derived ORR catalyst was prepared by pyrolyzing cobalt imidazolate frameworks (active Co-IM) at high temperatures, and significant progress has been achieved ever since (Ma et al., 2011). Among these, iron and carbon catalysts for ORR have been prepared from select MOFs (Li et al.). As catalysts derived from zinc-based MOFs have a wider distribution of pore sizes, iron-based MOFs such as MIL-88B-NH_3 have been used to develop carbonized nanoparticles through pyrolysis to reduce pore size distribution and produce metal active sites for high-performance ORR electrocatalysis (Zhao et al., 2014). For instance, catalysts have been developed from the pyrolysis of an iron-doped ZIF-8, a MOF containing both zinc and

iron coordination, with a uniform iron distribution in a nitrogen-doped carbon matrix, and exhibited apparent ORR activity and sufficient stability in 0.1 M $HClO_4$ (Wang et al., 2016). Among these, catalysts made up of iron carbide particles supported by carbon are of particular interest (Peng and Chen, 2018). In fact, ZIF-8 has been used as a template with pyrrole and iron(III) chloride to be heated at elevated temperatures to form iron carbide nanoparticles encapsulated in bamboo-like nitrogen doped nanotubes as ORR catalysts, where the FeN_x moieties and the carbon-encapsulated iron carbide were found to be responsible for the ORR activity, with a low hydrogen peroxide yield in both 0.1 M KOH and 0.5 M H_2SO_4 (Aijaz et al., 2017). In fact, catalysts with iron carbide active sites have been developed in the last several years (Luo et al., 2019, Zhao et al., 2016, Yang et al., 2017, Park et al., 2017, Song et al., 2018, Luo et al., 2018, Wang et al., 2019a).

To control the porosity of the resulting catalysts, carbon foams with hierarchical pores that consist of micro, meso and macropores are developed by solvent-assisted linker exchange before pyrolysis. For instance, when ZIF-8 was immersed in a 1H-1,2,3-triazole and methanol solution for three days, the resulting MOF yielded a catalyst that displayed an onset potential (E_{onset}) of -0.030 V versus Ag/AgCl in alkaline media and +0.570 V in acidic media, much better than that without exchange (Zhao et al., 2017). In another study (Hao et al., 2015), a boron and nitrogen co-doped porous carbon polyhedral catalyst was synthesized by treating pyrolyzed (800 °C) ZIF-11 with phenylboronic acid, sonication and drying before a second pyrolysis at 1000 °C, which showed the disappearance of micropores and a concurrent increase in mesoporosity during the boron doping process. Another approach taken is a dual template method where a monolith of ordered polystyrene spheres and solution of Pluronic F127 and iron(II and III) chloride is used to template the formation of macropores and mesopores, respectively, in a hierarchical structure

of porous spherical network of carbon (Wang et al., 2019b). These structures were adsorbed onto the surface of graphene to increase electrical conductivity and uplift ORR activity. Single site FeN_x moieties were distributed between the porous structures and the graphene sheet resulting in a catalyst with a higher activity than that of commercial Pt/C in 0.1 M KOH. Porous carbon has also been derived from pyrolysis of biomass (e.g., powdered cattle bones) with single iron atom sites promoted by a combination of iron(II) phthalocyanine and unsubstituted phthalocyanine resulting in a catalyst with similar onset potential and activity and enhanced stability, as compared to commercial Pt/C (Zhang et al., 2018).

Herein, a series of iron carbide@N-doped graphitic nanoparticles (FeNC) were pyrolytically derived from FeMOF-NH_2 with the same organic linkers but at different feeding ratios of the zinc and iron metal centers. The catalysts exhibited a similar prism geometry to the precursory MOFs, but with a porous graphitic surface. The evaporation of zinc compounds during pyrolysis increased the pore size and surface area, while graphitization of the MOF and encapsulation of Fe_3C nanoparticles occurred. An optimal zinc to iron feeding ratio in the MOF precursor was identified that resulted in a nanocarbon material with a desirable distribution of mesopores which facilitated the mass transfer and accessibility of catalytic active sites, hence leading to enhanced ORR performance.

Experimental Section

Chemicals. Iron(III) chloride hexahydrate ($FeCl_3$•$6H_2O$, 99.9%, Fisher Scientific), 2-aminoterepthalic acid (99%, Acros Organic), zinc chloride ($ZnCl_2$, 98%, Tokyo Chemical Industry), hydrochloric acid (HCl, 37%, Sigma-Aldrich), Pt/C (20 wt.%, Alfa Aesar), potassium hydroxide (KOH, Fisher Chemicals), and Nafion® 117 solution (~5% in a mixture of lower

aliphatic alcohols and water, Aldrich Chemistry) were all used as received. Water was supplied from a Barnstead Nanopure Water System (18.3 MΩ cm).

Sample preparation. The MOF precursors were synthesized by adopting a previously reported method (Bauer et al., 2008). In brief, 2-aminoterepthalic acid and $FeCl_3$ were mixed at a mass ratio of 1:3 by dissolving each into 5 mL of ultrapure water and then combing them into a 15 mL Teflon-lined autoclave and heated for 24 h at 110 °C. The sample was then filtered, washed with water, and dried at ambient temperature to produce an orange-red solid. Two additional MOFs were prepared in the same fashion except that a (mass) fraction of the iron(III) chloride hexahydrate was replaced with zinc chloride. The resulting samples were referred to FeMOF-NH_2-n (n = 1, 2 and 3, corresponding to 0, 20 and 30% Zn replacement in the MOF). To synthesize the ORR catalysts, the MOFs obtained above were ground by mortar and pestle and heated in a tube furnace (MTI GSL-1100X) under ultrahigh purity nitrogen at the flow rate of 200 $cm^3 \cdot min^{-1}$ at 900 °C for 1 h, producing a black flaky powder denoted as FeNC-n.

Characterization. X-ray diffraction (XRD) measurements were carried out with a Rigaku SmartLab Plus diffractometer with Cu K_α (λ = 1.54 Å) radiation operated at 40 kV and 44 mA. The XRD patterns of the MOF precursors were recorded from 2θ = 2° to 35° at the scan rate of 3° min^{-1} with the step size of 0.01°, and diffraction data of the ORR catalysts were collected from 2θ = 10° to 80° at the scan rate of 0.33° min^{-1} with the step size of 0.01°. Scanning electron microscopy (SEM) images were taken with a FEI Quanta 3D field emission microscope. Transmission electron microscopy (TEM) and elemental mapping images were taken with a Philips CM300 scope at 300 kV. X-ray photoelectron spectroscopy (XPS) measurements were taken with a PHI X-tool Instrument. Brunauer-Emmett-Teller (BET) surface area and pore volume analysis was carried out with a micropore size and chemisorption analyzer

(Quantachrom Autosorb). Raman spectra were collected with a Delta NU Raman 532 nm spectrometer.

Electrochemistry. Electrochemical measurements were conducted with a CHI 710C electrochemical workstation using a rotating gold ring-glassy carbon disk electrode (RRDE), a Ag/AgCl reference electrode, and a graphite rod counter electrode. The Ag/AgCl reference electrode was calibrated against a reversible hydrogen electrode (RHE) and all potentials in the study were referenced to this RHE. A catalyst ink was prepared by dispersing 1.0 mg of the FeNC catalysts prepared above in 1 mL of ethanol and 10 µL of Nafion by ultrasonication. 10 µL of the ink was then cast onto the glassy carbon electrode and allowed to dry in air. Then 3 µL of a Nafion:ethanol (v:v 1:4) solution was cast on top and allowed to dry, corresponding to a catalyst loading of 0.0407 $mg \cdot cm^{-2}$ on the disk electrode surface.

Results and Discussion

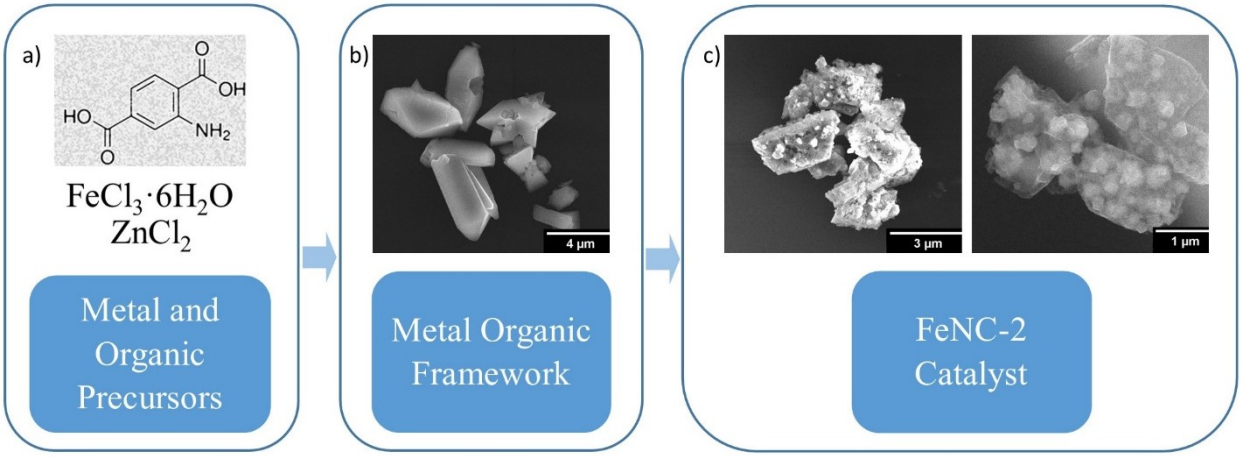

Figure 1. Schmatic diagram illustrating the synthesis of FeNC nanocomposites: a) metal salt and organic precursors used to synthesize FeMOF-NH_2; b) SEM image of FeMOF-NH_2-2 before pyrolysis; c) SEM image of the final product after pyrolysis, FeNC-2.

To investigate the effect of zinc content on the morphology and catalytic performances of the catalysts, three FeMOF-NH_2-n MOFs were prepared at different zinc feed ratios. Fig. 1 illustrates the synthesis from organic and salt precursors to the FeNC catalysts. From SEM measurements (Fig. 1b,c), the overall morphology of the FeNC-2 sample can be seen to resemble that of the FeMOF-NH_2-2 precursor. Additionally, the FeNC-2 catalyst consists of micrometer-scale porous carbon whose surface contains nanoparticles with a diameter of ca. 500 nm. Whereas the overall geometry of short prisms with pointed ends in the FeMOF-NH_2 is preserved during pyrolysis, the surface of FeNC-2 is more textured with folds along the surface and smaller particles below the surface. From Fig. 1c, it can be seen that FeCN-2 exhibits geometric carbon structures with particles embedded in the surface. This can be further manifested in TEM measurements (Fig. 2a,b) which clearly show that dense particles were encapsulated in a carbon matrix. EDX elemental mapping (Fig. 3) reveals that the nanoparticles under the surface of FNC-2 are of an iron compound and confirms the surrounding material as graphitic carbon with oxygen and nitrogen throughout. Indeed, from HRTEM measurements (Fig. 2c,d), the sample can be seen to exhibit well-defined lattice fringes with the interplanar spacing varying from 3.10 Å to 3.95 Å. This is attributed to graphitic (002) carbon where the d spacing expands somewhat, as compared to that of pristine graphite, because of thermal treatment at elevated temperatures (Akhavan, 2010). The 6.28 Å Moiré fringe is due to interference from overlapping interlayer spacings (Tu et al., 2017). Taken together, results from the SEM and TEM studies show that pyrolysis of the MOF precursors yielded iron and nitrogen codoped carbon which contained iron nanoparticles encapsulated within a graphitic shell.

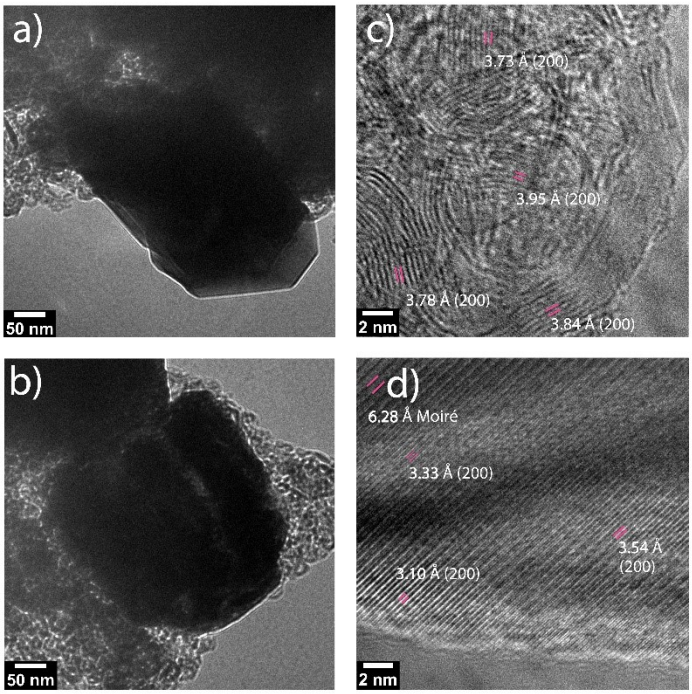

Figure 2. (a, b) TEM and (c, d) HRTEM images of FeCN-2 showcasing the well-defined lattice fringes.

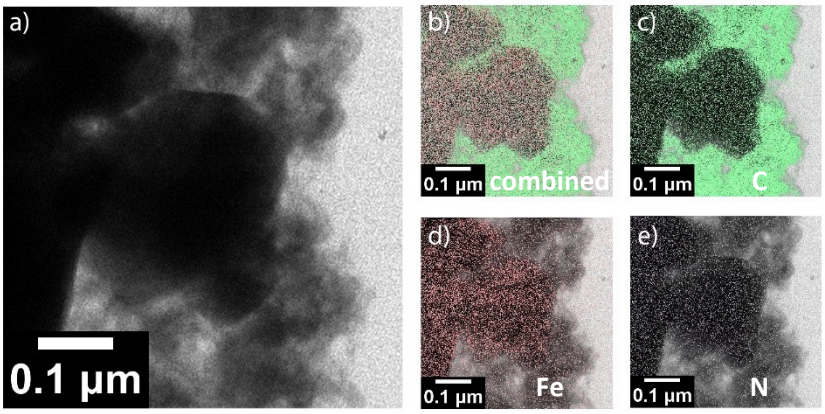

Figure 3. a) TEM image of FeCN-2, with the corresponding elemental maps of b) combined elements, c) carbon, d) iron, and e) nitrogen.

All as-synthesized FeMOF-NH_2-n MOFs show the characteristic XRD patterns corresponding to those of Fe-MIL-53-NH_2 at 2θ = 6.86°, 8.86°, 17.1° and 26.5°, as reported previously (Bauer et al.). Note that the XRD patterns remained unchanged as the feed ratio of zinc increased, suggesting the crystalline characteristics of the MOFs were not affected by the

incorporation of zinc. Fig. 4 depicts the corresponding XRD patterns of the FeNC samples prepared by pyrolysis of the FeMOF-NH_2-n MOFs. One can see that all samples show a sharp diffraction peak at 26.1°, which can be assigned to the (002) plane of graphitic carbon, and the peaks at 43.8°, 44.7° and 50.8° could be assigned to cementite (Fe_3C, G23753) and magnetite (Fe_3O_4, AMCSD 0002400) (Wood et al., 2004, Haavik et al., 2000). These results indicated that graphitic carbon, Fe_3C, and Fe_3O_4 were formed in the FeNC nanocomposites. Using the Scherrer equation, $\tau = \frac{K\lambda}{\beta \cos\theta}$, the mean size of the crystalline domains was estimated to be about 39 nm for the iron carbide assuming a *K* constant of 0.9. Since this is much smaller than the 500 nm particles seen in TEM measurements (Figure 2), the result indicates that the particles most likely contained a polycrystalline structure.

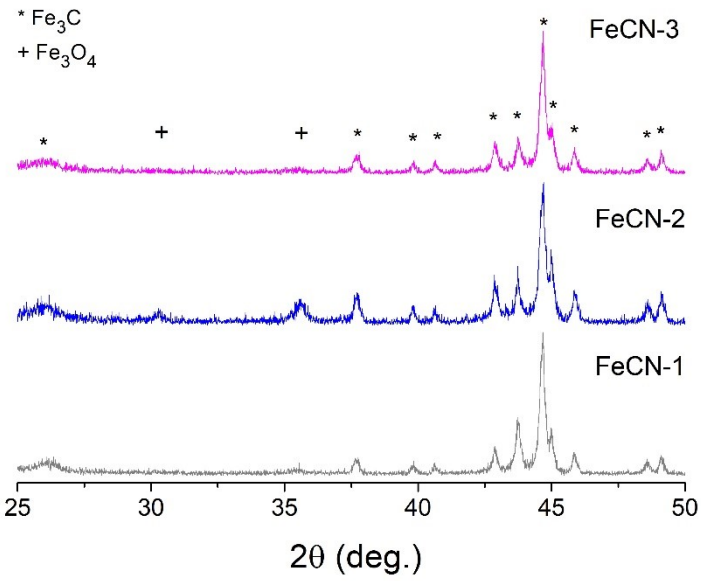

Figure 4. PXRD patterns of the FeNC Catalysts.

The elemental composition and valence state of the samples were then examined by XPS measurements. From the survey spectra, the C, N, Fe and O elements can all be clearly defined

in the series of FeNC samples, suggesting that indeed Fe and N were successfully doped into the carbon skeletons. The high-resolution scans of the C 1s electrons are depicted in Fig. 5a. For the FeNC-1 and FeNC-2 samples, deconvolution yields a peak at 283 eV due to carbon in Fe_3C, sp^2 C at 284 eV and sp^3 C at 285 eV, with the peak at 286 eV indicative of C-O (Gautam et al., 2018, Furlan et al., 2015, Lu et al., 2017, Chen et al., 2016, Ali et al., 2017). For FeNC-3, however, this C=O carbon cannot be resolved, and instead there is an additional peak of carbonate (Ali et al., 2017, Bhattacharya et al., 1997).

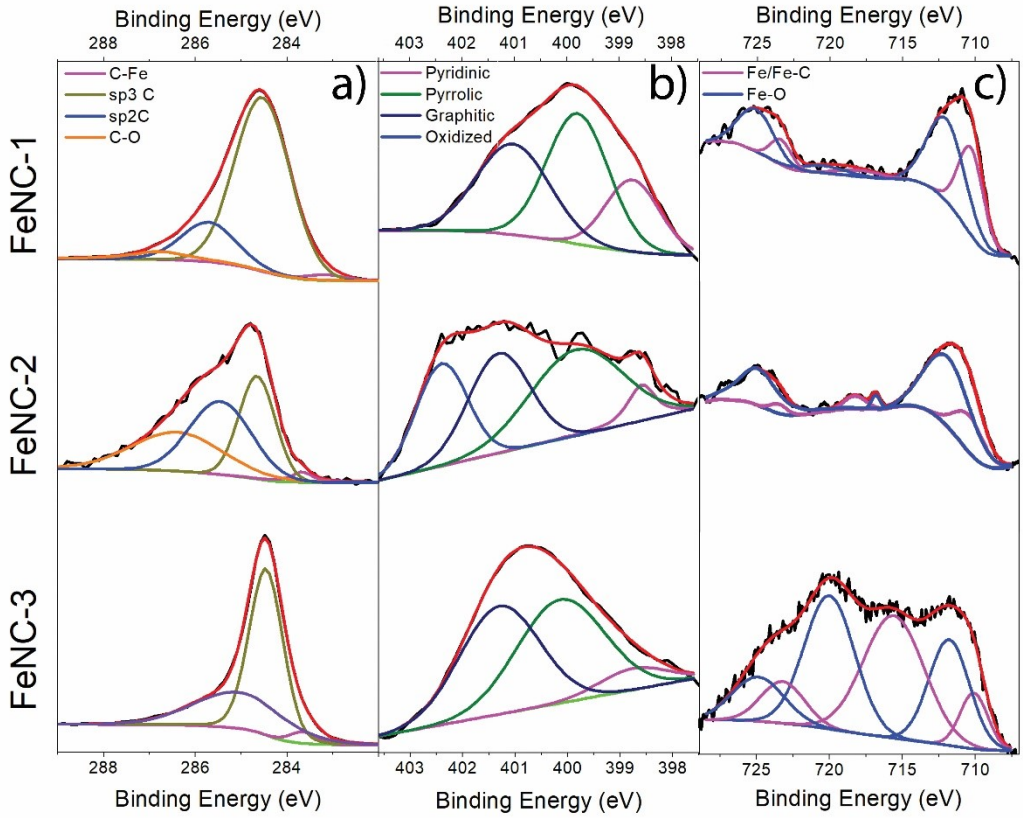

Figure 5. High-resolution XPS scans of the a) C 1s, b) N 1s, and c) Fe 2p electrons in the FeNC nanocomposites. Black curves are raw data, and colored curves are deconvolution fits, as specified in the legends.

The N 1s scans are shown in Fig. 5b. All three FeNC samples can be seen to include peaks at 399, 400, and 401 eV, which are assigned to pyridinic, pyrrolic, and graphitic nitrogen, respectively, confirming the successful doping of nitrogen into the carbon matrices (Lu et al.,

2017). From Table 1, one can see that nitrogen accounted for 0.58 at% for FeNC-1, 1.52 at% for FeNC-2 and 0.56 at% for FeNC-3. That is, FeNC-2 contained the highest concentration of N dopants among the series.

The corresponding Fe 2p spectra are depicted in Fig. 5c. One can see that the binding energy of Fe 2p in Fe-C decreased in the order of FeNC-1 (710.4 eV) ≈ FeNC-2 (710.4 eV) > FeNC-3 (710.2 eV), whereas the corresponding C 1s binding energy increased in the order of FeNC-1 (283.2 eV) < FeNC-2 (283.6 eV) < FeNC-3 (283.8 eV), indicative of increasing carbon to iron charge transfer from FeNC-1 to FeNC-2 and to FeNC-3 (Table S1) (Yamashita and Hayes, 2008, Lin et al., 2014, Wu et al., 2015). In addition, FeNC-2 can be seen to have the least amount of iron at 0.80 at%, less than half of those of FeNC-1 and FeNC-3, but have the greatest nitrogen to iron ratio. In fact, FeNC-2 has the highest concentration of Fe-C bonds, which is conducive to ORR electrocatalysis.

Table 1. Elemental compositions by XPS measurements

Sample	**Carbon**	**Iron**	**Nitrogen**	**Oxygen**
FeCN-1	79.7 at%	2.64 at%	0.58 at%	17.1 at%
FeCN-2	82.5 at%	0.80 at%	1.52 at%	15.2 at%
FeCN-3	88.0 at%	1.60 at%	0.56 at%	9.85 at%

The porosity and surface area of the samples were then examined by nitrogen adsorption-desorption measurements. FeNC-2 exhibited a type IV isotherm with an H3 hysteresis loop, typical of capillary condensation in mesopores in the form of aggregates of plate like particles giving rise to slit shaped pores (Sing et al., 1985). The FeMOF-NH_2-2 precursor exhibits a surface area of 261 $m^2 \cdot g^{-1}$ by the density functional theory (DFT) method and 433 $m^2 \cdot g^{-1}$ from multi-point BET, a half pore width of 2.18 nm, and a pore volume of 0.415 $cm^3 \cdot g^{-1}$. After

pyrolysis at 900 °C for 1 h, the resulting catalyst (FeNC-2) shows a specific surface area of 746.0 $m^2 \cdot g^{-1}$ by the DFT method and 771 $m^2 \cdot g^{-1}$ from multi-point BET (Fig. 6b), a half pore width of 2.38 nm, and a pore volume of 1.267 $cm^3 \cdot g^{-1}$, suggesting drastic enhancement of the porosity. This is largely due to the low boiling point (volatility) of the zinc compounds in FeMOF-NH_2, which acted as an activating agent by evaporating out of the structure during pyrolysis creating pores in the carbon skeletons.

For comparison, from BET measurements (Fig. 6b), FeNC-1 has a surface area of 189.2 $m^2 \cdot g^{-1}$ by the DFT method and 213.5 $m^2 \cdot g^{-1}$ from multi-point BET, a half pore width of 1.692 nm, and a pore volume of 0.242 $cm^3 \cdot g^{-1}$. FeNC-3 has a surface area of 607.7 $m^2 g^{-1}$ by the DFT method and 557.4 $m^2 \cdot g^{-1}$ from multi-point BET, a half pore width of 1.970 nm, and a pore volume of 0.773 $cm^3 \cdot g^{-1}$. Interestingly, FeNC-2 exhibited a larger surface area and pore volume than FeNC-3, whereas FeNC-1 has the smallest surface area and pore volume. During pyrolysis, zinc acted as the activating agent in the FeMOF-NH_2 precursors creating porosity in FeNC. As FeMOF-NH_2-1 lacks zinc, this activation was not present during pyrolysis resulting in the smallest surface area, pore width and volume. This is consistent with both FeNC-2 and FeNC-3 having a significantly higher surface area and pore volume than FeNC-1, with FeNC-2 having the highest surface area, pore volume and half-pore width overall. Furthermore, the fact that FeNC-3 displayed a smaller surface area and pores than FeNC-2 suggests that there is an optimal amount of zinc in the feeding ratio for the creation of larger pores.

To further understand porosity of these samples, the pore size distributions can be observed in the Barrett-Joyner-Halenda (BJH) plots in Fig. 6a. The distribution of FeNC-2 peaks broadly at 2.38 nm with no features below 2 nm. There is negligible presence of micropores in FeNC-2. The broad peak indicates a wide and continuous distribution of pore sizes. The

distribution of FeNC-3 lacks this peak and instead peaks at 1.00 nm, 1.97 nm (both micropores) and 2.78 nm. These three narrow peaks indicate a trimodal distribution of pore sizes that are non-continuous. FeNC-1 has smaller broad peaks at 0.65 nm and 1.85 nm and thus only contains micropores. From the peak intensities, FeNC-1 appears as the least porous sample. The different pore size distributions for each of the samples indicates that the zinc feeding ratio affects not just the surface area, pore volumes and mode pore widths, but the distribution in width, intensity and width centers. An optimal zinc feeding ratio is required for a broad distribution around a single center.

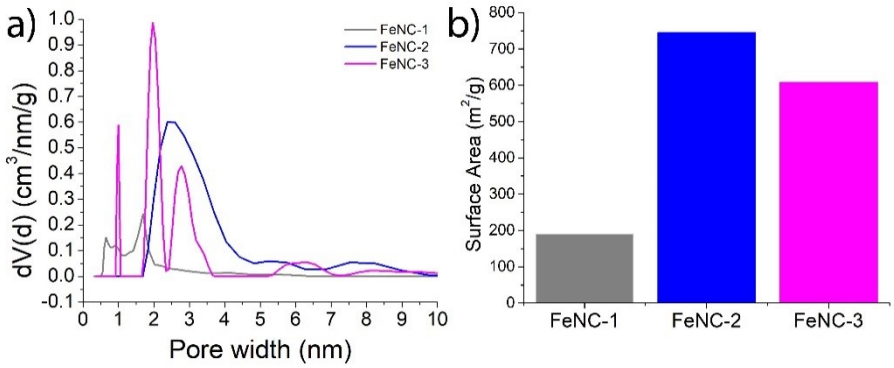

Figure 6. a) BJH plots of the FeNC series. b) Surface area obtained from the DFT method.

Table 2 Summary of the analysis of BET results

	DFT Method			**MP BET**
Sample	Pore Volume ($cm^3 \cdot g^{-1}$)	Surface Area ($m^2 \cdot g^{-1}$)	Half Pore Width (nm)	Surface Area ($m^2 \cdot g^{-1}$)
FeNC-1	0.242	189.2	1.69	176.2
FeNC-2	1.267	745.6	2.38	914.3
FeNC-3	0.773	607.7	1.97	682.7

In the Raman spectra for the FeNC series, the ratio of the D-band to G-band intensities (I_D/I_G,) was estimated to be 1.82 for FeNC-1, 1.35 for FeNC-2 and 1.38 for FeNC-3, suggesting that the addition of zinc into the precursor facilitated graphitization of the samples.

The electrocatalytic activity towards ORR was then quantitatively assessed by electrochemical measurements. From the RRDE voltammograms in Fig. 7a, apparent ORR activity can be seen for all samples, but the activity varies among the series. For instance, for FeNC-1, the onset potential (E_{onset}) was identified at +0.813 V vs RHE and the limiting current at 1.5 $mA \cdot cm^{-2}$; for FeNC-2, it is +0.993 V vs RHE and 1.3 $mA \cdot cm^{-2}$, and +0.704 V vs RHE and 0.91 $mA \cdot cm^{-2}$ for FeNC-3. One can see that FeNC-2 stood out as the best among the series, with an onset potential close to that of Pt/C (+0.993 V). In the corresponding Tafel plots in Fig. 7b, the slopes are estimated to be -59.0 $mV \cdot dec^{-1}$, -61.4 $mV \cdot dec^{-1}$, -39.9 $mV \cdot dec^{-1}$, and -4.9 $mV \cdot dec^{-1}$ for FeNC-1, FeNC-2, FeNC-3, and Pt/C 20%, respectively. All samples can be seen to show an increase of the kinetic current with an increase of overpotential, and within the potential range of +0.45 to +0.90 V, FeNC-2 exhibited the highest kinetic current. For instance, at +0.80 V, the kinetic current density was 12.5 $\mu A \cdot cm^{-2}$, 640 $\mu A \cdot cm^{-2}$ and 0.819 $\mu A \cdot cm^{-2}$ for FeNC-1, FeNC-2, and FeNC-3, respectively. This, again, shows that the FeNC-2 sample was the best catalyst among the FeNC series. Consistent behaviors were observed in the analysis of the number of electron transfer involved (n), $n = \frac{4I_{Disk}}{I_{Disk}+I_{Ring}/N}$, where I_{Disk} and I_{Ring} are the voltammetric currents at the disk and ring, respectively, and N is the collection efficiency (37%). The results are summarized in Fig. 7c. All FeNC samples showed an n number of at least 3.3, indicating that oxygen was mostly reduced to OH^- through the four-electron pathway.

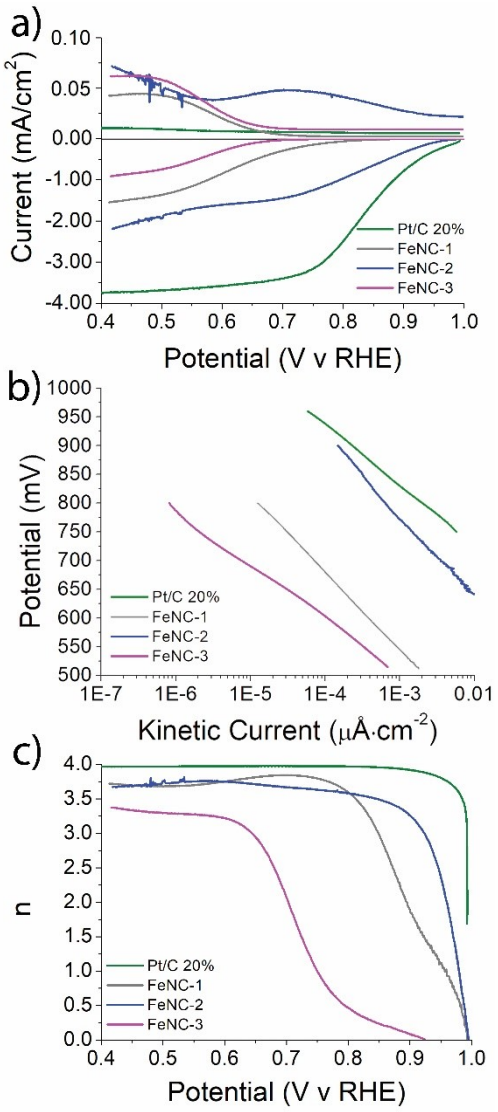

Figure 7. a) RRDE voltammograms of FeNC catalysts at a rotation rate of 2500 RPM and potential scan rate of 10 mV·s^{-1} in oxygen saturated 0.1 M KOH. Top: ring current density. Bottom: disk current density. b) Tafel plot of FeNC catalysts. c) Plot of the number of electrons transferred (n) versus electrode potential.

The effect of pyrolysis temperature on the FeMOF-NH_2-2 derived catalyst was also explored by pyrolyzing the FeMOF-NH_2-2 precursor at 700 and 800 °C, labeled as FeNC-2-700 and FeNC-2-800, respectively (Fig. 8). One can see that FeNC-2-700 and FeNC-2-800 have an onset potential of +0.785 V vs RHE, almost 0.2 V more negative than that of FeNC-2 (prepared at 900 °C). In addition, FeNC-2-700 and FeNC-2-800 showed a limiting current density of 1.1 mA·cm^{-2} and 1.4 mA·cm^{-2} and kinetic current density of 7.60 μA·cm^{-2} and 5.20 μA·cm^{-2},

respectively, also markedly lower than that of FeNC-2. The lack of improvement in activity with the decrease in pyrolysis temperature illustrates the necessity of high temperature in pyrolytic preparation of the nanocomposites. FeNC-2 was also etched with 12 M hydrochloric acid overnight to evaluate the activity of the catalyst without any surface particles. The onset potential of FeNC-2 worsened after etching with acid, indicating the importance of particles on the surface in the reduction of oxygen.

In deriving porous nitrogen doped carbon catalysts from FeMOF-NH_2-2, a nanocarbon structure with accessible surface iron carbide nanoparticles with high ORR activity is formed. The inclusion of zinc in the MOF has a positive effect on the final catalysts attained through pyrolysis. Increasing the amount of zinc in the precursory MOF has noticeable benefits on the design of the carbon catalyst up to FeMOF-NH_2-2. The pore width increased from 3.384 nm to 4.764 nm, as did the surface area (189.2 $m^2 \cdot g^{-1}$ to 745.6 $m^2 \cdot g^{-1}$) and pore volume (0.242 $cm^3 \cdot g^{-1}$ to 1.267 $cm^3 \cdot g^{-1}$), making the surface more accessible. Of the FeNC catalysts, FeNC-2 has the highest activity, in coincidence with the highest concentration of Fe-C (Table S1), highlighting the importance of the surface structural engineering in improving the catalytic activity. In addition, there is a positive correlation between the variables of pore structure (pore volume, pore width, and surface area), most probably because the increase in pore volume and pore width results in increased exposure of active sites. Without this activation, the surface is highly microporous and unsuitable for mass transfer and renders surface active sites less accessible to the reaction despite the higher concentration of iron species. Instead, FeNC-2 has a wide distribution of mesopores with a mean of 2.33 nm and mode of 2.38 nm which is conducive to mass transfer in ORR. When excess zinc was incorporated into FeMOF-NH_2, the evaporation of zinc chloride during pyrolysis became increasingly destructive, decreasing the surface area and

changing the nature of the pores. This prevented the formation of abundant mesopores with a mode of 2.38 nm and resulted in a trimodal distribution and lower mode pore width of 1.97 nm, leading to dampened activity. Taken together, these results suggest that the maximal ORR activity of FeNC-2 among the series is likely the combined consequence of high Fe-C bonding moieties and optimal porosity.

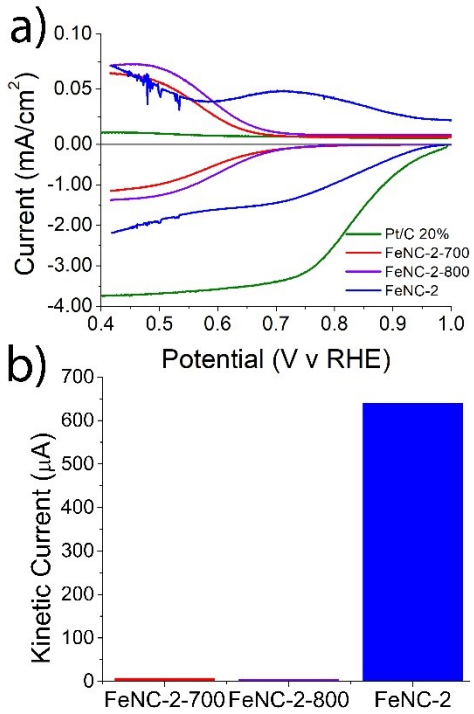

Figure 8. a) RRDE voltammograms of FeNC-2 prepared by pyrolysis of FeMOF-NH_2-2 at varying temperatures at a rotation rate of 2500 RPM and potential scan rate of 10 mV/s in oxygen saturated 0.1 M KOH. Top: Ring current density. Bottom: Disk current density b) Column plot comparing the kinetic current for each sample at +0.8 V.

Notably, in comparison to relevant porous Fe,N-codoped C catalysts reported in the literature (Aijaz et al., 2017, Wang et al., 2019a, Luo et al., 2018, Song et al., 2018, Park et al., 2017, Yang et al,, 2017, Zhao et al., 2016, Luo et al., 2019), FeNC-2 shows an onset potential (+0.997 V vs RHE) that is either more positive or comparable to the literature results. In addition, FeNC-2 has a larger surface area (745.62 $m^2 \cdot g^{-1}$) than several reported porous Fe_3C/C catalysts (Zhao et al., 2017, Wang et al., 2019b, Zhang et al., 2018, Wang et al., 2016, Xiao et

al., 2018). Pore size distribution is also important. The generally smaller mesopores (2.38 nm) of FeNC-2 are advantageous in ORR electrocatalysis, in conjunction with the larger pore volume.

Summary

In this study, a series of mesoporous iron carbide@graphitic nanoparticles were derived by controlled pyrolysis of FeMOF-NH_2 at different zinc feeding ratios in the MIL-53-NH_2 synthesis. The pyrolysis was shown to not only graphitize the MOF and form Fe_3C particles, but to evaporate the zinc compound to form pores whose nature were dependent on the feed ratio. Through BET analysis, the optimal catalyst (FeNC-2) was shown to lack micropores and possess a distribution of small mesopores centered on 2.33 nm with a mode of 2.38 nm resulting in an ORR activity that is better or comparable to other Fe-N-C catalysts in the literature. The impact of this simple yet crucial synthetic parameter presents an opportunity for further surface engineering of nanocarbon catalysts through the tuning of inorganic precursors.

Acknowledgments This work was supported in part by the National Science Foundation (CHE-1710408 and CHE-1900235) and a Special Research Grant from the UCSC. TEM and XPS work was carried out at the National Center for Electron Microscopy and Molecular Foundry, Lawrence Berkeley National Laboratory, which is supported by the US Department of Energy, as part of a user project.

References

AIJAZ, A., MASA, J., RÖSLER, C., ANTONI, H., FISCHER, R. A., SCHUHMANN, W. & MUHLER, M. 2017. MOF‐Templated Assembly Approach for Fe3C Nanoparticles Encapsulated in Bamboo‐Like N‐Doped CNTs: Highly Efficient Oxygen Reduction under both Acidic and Basic Conditions. *Chem. Eur. J.,* 23, 12125-12130.

AKHAVAN, O. 2010. The effect of heat treatment on formation of graphene thin films from graphene oxide nanosheets. *Carbon,* 48**,** 509-519.

ALI, H., ZAMAN, S., MAJEED, I., KANODARWALA, F. K., NADEEM, M. A., STRIDE, J. A. & NADEEM, M. A. 2017. Porous Carbon/rGO Composite: An Ideal Support Material of Highly Efficient Palladium Electrocatalysts for the Formic Acid Oxidation Reaction. *Chemelectrochem,* 4**,** 3126-3133.

BAUER, S., SERRE, C., DEVIC, T., HORCAJADA, P., MARROT, J., FEREY, G. & STOCK, N. 2008. High-throughput assisted rationalization of the formation of metal organic frameworks in the iron(III) aminoterephthalate solvothermal system. *Inorg. Chem.,* 47**,** 7568-7576.

BHATTACHARYA, A. K., PYKE, D. R., WALKER, G. S. & WERRETT, C. R. 1997. The surface reactivity of different aluminas as revealed by their XPS Cls spectra. *Appl. Surf. Sci.,* 108**,** 465-470.

CHEN, L. M., HU, P. G., DEMING, C. P., WANG, N., LU, J. E. & CHEN, S. W. 2016. Intervalence Charge Transfer of Ruthenium-Nitrogen Moieties Embedded within Nitrogen-Doped Graphene Quantum Dots. *J. Phys. Chem. C,* 120**,** 13303-13309.

CHEN, M., JIANG, Y., MEI, P., ZHANG, Y., ZHENG, X. F., XIAO, W., YOU, Q. L., YAN, X. M. & TANG, H. L. 2019a. Polyacrylamide Microspheres-Derived Fe3C@N-doped Carbon Nanospheres as Efficient Catalyst for Oxygen Reduction Reaction. *Polymers,* 11, 767.

CHEN, P., WANG, L.-K., WANG, G., GAO, M.-R., GE, J., YUAN, W.-J., SHEN, Y.-H., XIE, A.-J. & YU, S.-H. 2014. Nitrogen-doped nanoporous carbon nanosheets derived from plant biomass: an efficient catalyst for oxygen reduction reaction. *Energy Environ. Sci.,* 7**,** 4095-4103.

CHEN, X., XU, J. Y., CHAI, H., WANG, Y. C., JIA, D. Z. & ZHOU, W. Y. 2019b. One-step synthesis of hollow chain-like nitrogen doped carbon nanotubes/iron carbide as highly efficient bifunctional oxygen electrocatalyst. *J. Electroanal. Chem.,* 838**,** 16-22.

FERRANDON, M., KROPF, A. J., MYERS, D. J., ARTYUSHKOVA, K., KRAMM, U., BOGDANOFF, P., WU, G., JOHNSTON, C. M. & ZELENAY, P. 2012. Multitechnique characterization of a polyaniline–iron–carbon oxygen reduction catalyst. *J. Phys. Chem. C,* 116**,** 16001-16013.

FURLAN, A., JANSSON, U., LU, J., HULTMAN, L. & MAGNUSON, M. 2015. Structure and bonding in amorphous iron carbide thin films. *J. Phys.-Condens. Matter,* 27, 045002.

GAUTAM, J., THANH, T. D., MAITI, K., KIM, N. H. & LEE, J. H. 2018. Highly efficient electrocatalyst of N-doped graphene-encapsulated cobalt-iron carbides towards oxygen reduction reaction. *Carbon,* 137**,** 358-367.

HAAVIK, C., STOLEN, S., FJELLVAG, H., HANFLAND, M. & HAUSERMANN, D. 2000. Equation of state of magnetite and its high-pressure modification: Thermodynamics of the Fe-O system at high pressure. *Am Min.,* 85**,** 514-523.

HAO, F., YAO, Y., LI, Y. P., TIAN, C. X., ZHANG, X. H. & CHEN, J. H. 2015. Synthesis of high-concentration B and N co-doped porous carbon polyhedra and their supercapacitive properties. *Rsc Adv.,* 5**,** 77527-77533.

HU, P. G., LIU, K., DEMING, C. P. & CHEN, S. W. 2015. Multifunctional graphene-based nanostructures for efficient electrocatalytic reduction of oxygen. *J. Chem. Technol. Biotechnol.,* 90**,** 2132-2151.

HU, Y., JENSEN, J. O., ZHANG, W., CLEEMANN, L. N., XING, W., BJERRUM, N. J. & LI, Q. F. 2014. Hollow Spheres of Iron Carbide Nanoparticles Encased in Graphitic Layers as Oxygen Reduction Catalysts. *Angew. Chem.-Int. Edit.,* 53**,** 3675-3679.

LEFEVRE, M., PROIETTI, E., JAOUEN, F. & DODELET, J. P. 2009. Iron-Based Catalysts with Improved Oxygen Reduction Activity in Polymer Electrolyte Fuel Cells. *Science,* 324**,** 71-74.

LI, L. J., HE, J. X., WANG, Y., LV, X. X., GU, X., DAI, P. C., LIU, D. D. & ZHAO, X. B. 2019. Metal-organic frameworks: a promising platform for constructing non-noble electrocatalysts for the oxygen-reduction reaction. *J. Mater. Chem. A,* 7**,** 1964-1988.

LIN, L., ZHU, Q. & XU, A. W. 2014. Noble-Metal-Free Fe-N/C Catalyst for Highly Efficient Oxygen Reduction Reaction under Both Alkaline and Acidic Conditions. *J. Am. Chem. Soc.,* 136**,** 11027-11033.

LIU, Y. X., LI, T. F., CAO, X. Y., LIU, J. J., ZHANG, J., JIA, J., WANG, F. & PAN, K. 2019. Electrospun Fe2C-loaded carbon nanofibers as efficient electrocatalysts for oxygen reduction reaction. *Nanotechnology,* 30, 325403.

LU, B. Z., GUO, L., WU, F., PENG, Y., LU, J. E., SMART, T. J., WANG, N., FINFROCK, Y. Z., MORRIS, D., ZHANG, P., LI, N., GAO, P., PING, Y. & CHEN, S. W. 2019. Ruthenium atomically dispersed in carbon outperforms platinum toward hydrogen evolution in alkaline media. *Nat. Commun.,* 10, 631.

LU, B. Z., SMART, T. J., QIN, D. D., LU, J. E., WANG, N., CHEN, L. M., PENG, Y., PING, Y. & CHEN, S. W. 2017. Nitrogen and Iron-Codoped Carbon Hollow Nanotubules as High-Performance Catalysts toward Oxygen Reduction Reaction: A Combined Experimental and Theoretical Study. *Chem. Mater.,* 29**,** 5617-5628.

LUO, Y., ZHANG, J., CHEN, Y. H., LI, Z. J., CHEN, J. W., WANG, G. & WANG, R. L. 2019. MOF-derived porous carbon supported iron-based catalysts with optimized active sites towards oxygen reduction reaction. *J. Electroanal. Chem.,* 847, 113191.

LUO, Y., ZHANG, J., KIANI, M., CHEN, Y. H., CHEN, J. W., WANG, G., CHAN, S. H. & WANG, R. L. 2018. Synthesis of MOF-Derived Nonprecious Catalyst with High Electrocatalytic Activity for Oxygen Reduction Reaction. *Ind. Eng. Chem. Res.,* 57**,** 12087-12095.

MA, S. Q., GOENAGA, G. A., CALL, A. V. & LIU, D. J. 2011. Cobalt Imidazolate Framework as Precursor for Oxygen Reduction Reaction Electrocatalysts. *Chem. Eur. J.,* 17**,** 2063-2067.

OZOEMENA, K. I. 2016. Nanostructured platinum-free electrocatalysts in alkaline direct alcohol fuel cells: catalyst design, principles and applications. *Rsc Adv.,* 6**,** 89523-89550.

PARK, J., LEE, H., BAE, Y. E., PARK, K. C., JI, H., JEONG, N. C., LEE, M. H., KWON, O. J. & LEE, C. Y. 2017. Dual-Functional Electrocatalyst Derived from Iron-PorphyrinEncapsulated Metal-Organic Frameworks. *Acs Appl. Mater. Interfaces,* 9**,** 28758-28765.

PENG, Y. & CHEN, S. W. 2018. Electrocatalysts Based on Metal@Carbon Core@Shell Nanocomposites: an Overview. *Green Energy Environ.,* 3**,** 335-351.

PENG, Y., LU, B. Z. & CHEN, S. W. 2018. Carbon-Supported Single Atom Catalysts for Electrochemical Energy Conversion and Storage. *Adv. Mater.,* 30, 1801995.

SING, K. S. W., EVERETT, D. H., HAUL, R. A. W., MOSCOU, L., PIEROTTI, R. A., ROUQUEROL, J. & SIEMIENIEWSKA, T. 1985. Reporting Physisorption Data for Gas Solid Systems with Special Reference to the Determination of Surface-Area and Porosity (Recommendations 1984). *Pure Appl. Chem.,* 57**,** 603-619.

SONG, C. S., WU, S. K., SHEN, X. P., MIAO, X. L., JI, Z. Y., YUAN, A. H., XU, K. Q., LIU, M. M., XIE, X. L., KONG, L. R., ZHU, G. X. & SHAH, S. A. 2018. Metal-organic framework derived Fe/Fe3C@N-doped-carbon porous hierarchical polyhedrons as bifunctional electrocatalysts for hydrogen evolution and oxygen-reduction reactions. *J. Colloid Interface Sci.,* 524**,** 93-101.

TAN, H. B., LI, Y. Q., KIM, J., TAKEI, T., WANG, Z. L., XU, X. T., WANG, J., BANDO, Y., KANG, Y. M., TANG, J. & YAMAUCHI, Y. 2018. Sub-50 nm Iron-Nitrogen-Doped Hollow Carbon Sphere-Encapsulated Iron Carbide Nanoparticles as Efficient Oxygen Reduction Catalysts. *Adv. Sci.,* 5, 1800120.

TAN, H. B., TANG, J., KIM, J., KANETI, Y. V., KANG, Y. M., SUGAHARA, Y. & YAMAUCHI, Y. 2019. Rational design and construction of nanoporous iron- and nitrogen-doped carbon electrocatalysts for oxygen reduction reaction. *J. Mater. Chem. A,* 7**,** 1380-1393.

TU, J. F., RAJULE, N., LIU, Y. & MARTIN, J. 2017. Nanostructure diffraction analysis of a copper/single walled carbon nanotube nanocomposite synthesized by Laser Surface Implanting. *Carbon,* 113**,** 1-9.

WANG, H., YIN, F. X., LIU, N., KOU, R. H., HE, X. B., SUN, C. J., CHEN, B. H., LIU, D. J. & YIN, H. Q. 2019a. Engineering Fe-Fe3C@Fe-N-C Active Sites and Hybrid Structures from Dual Metal-Organic Frameworks for Oxygen Reduction Reaction in H-2-O-2 Fuel Cell and Li-O-2 Battery. *Adv. Funct. Mater.,* 29, 1901531.

WANG, S. H., YAN, X., WU, K. H., CHEN, X. M., FENG, J. M., LU, P. Y., FENG, H., CHENG, H. M., LIANG, J. & DOU, S. X. 2019b. A hierarchical porous Fe-N impregnated carbon-graphene hybrid for high-performance oxygen reduction reaction. *Carbon,* 144**,** 798-804.

WANG, X. J., ZHANG, H. G., LIN, H. H., GUPTA, S., WANG, C., TAO, Z. X., FU, H., WANG, T., ZHENG, J., WU, G. & LI, X. G. 2016. Directly converting Fe-doped metal organic frameworks into highly active and stable Fe-N-C catalysts for oxygen reduction in acid. *Nano Energy,* 25**,** 110-119.

WANG, Y., LI, J. & WEI, Z. D. 2018. Recent Progress of Carbon-Based Materials in Oxygen Reduction Reaction Catalysis. *Chemelectrochem,* 5**,** 1764-1774.

WOOD, I. G., VOCADLO, L., KNIGHT, K. S., DOBSON, D. P., MARSHALL, W. G., PRICE, G. D. & BRODHOLT, J. 2004. Thermal expansion and crystal structure of cementite, Fe(3)C, between 4 and 600 K determined by time-of-flight neutron powder diffraction. *J. Appl. Crystallogr.,* 37**,** 82-90.

WU, Z. Y., XU, X. X., HU, B. C., LIANG, H. W., LIN, Y., CHEN, L. F. & YU, S. H. 2015. Iron Carbide Nanoparticles Encapsulated in Mesoporous Fe-N-Doped Carbon Nanofibers for Efficient Electrocatalysis. *Angew. Chem.-Int. Edit.,* 54**,** 8179-8183.

XIAO, M. L., ZHU, J. B., FENG, L. G., LIU, C. P. & XING, W. 2015. Meso/Macroporous Nitrogen-Doped Carbon Architectures with Iron Carbide Encapsulated in Graphitic Layers as an Efficient and Robust Catalyst for the Oxygen Reduction Reaction in Both Acidic and Alkaline Solutions. *Adv. Mater.,* 27**,** 2521-2527.

XIAO, M. L., ZHU, J. B., MA, L., JIN, Z., GE, J., DENG, X. J., HOU, Y., HE, Q. G., LI, J. K., JIA, Q. Y., MUKERJEE, S., YANG, R., JIANG, Z., SU, D. S., LIU, C. P. & XING, W. 2018. Microporous Framework Induced

Synthesis of Single-Atom Dispersed Fe-N-C Acidic ORR Catalyst and Its in Situ Reduced Fe-N-4 Active Site Identification Revealed by X-ray Absorption Spectroscopy. *Acs Catal.,* 8**,** 2824-2832.

YAMASHITA, T. & HAYES, P. 2008. Analysis of XPS spectra of Fe2+ and Fe3+ ions in oxide materials. *Appl. Surf. Sci.,* 254**,** 2441-2449.

YANG, L. M., BAI, Y. Z., ZHANG, H. J., GENG, J. T., SHAO, Z. G. & YI, B. L. 2017. Nitrogen-doped porous carbon derived from Fe-MIL nanocrystals as an electrocatalyst for efficient oxygen reduction. *Rsc Adv.,* 7**,** 22610-22618.

ZHANG, X. R., MOLLAMAHALE, Y. B., LYU, D. D., LIANG, L. Z., YU, F., QING, M., DU, Y. H., ZHANG, X. Y., TIAN, Z. Q. & SHEN, P. K. 2019. Molecular-level design of Fe-N-C catalysts derived from Fe-dual pyridine coordination complexes for highly efficient oxygen reduction. *J. Catal.,* 372**,** 245-257.

ZHANG, Z. P., SUN, J. T., WANG, F. & DAI, L. M. 2018. Efficient Oxygen Reduction Reaction (ORR) Catalysts Based on Single Iron Atoms Dispersed on a Hierarchically Structured Porous Carbon Framework. *Angew. Chem.-Int. Edit.,* 57**,** 9038-9043.

ZHAO, P. P., HUA, X., XU, W., LUO, W., CHEN, S. L. & CHENG, G. Z. 2016. Metal-organic framework-derived hybrid of Fe3C nanorod-encapsulated, N-doped CNTs on porous carbon sheets for highly efficient oxygen reduction and water oxidation. *Catal. Sci. Technol.,* 6**,** 6365-6371.

ZHAO, R., XIA, W., LIN, C., SUN, J. L., MAHMOOD, A., WANG, Q. F., QIU, B., TABASSUM, H. & ZOU, R. Q. 2017. A pore-expansion strategy to synthesize hierarchically porous carbon derived from metal-organic framework for enhanced oxygen reduction. *Carbon,* 114**,** 284-290.

ZHAO, S. L., YIN, H. J., DU, L., HE, L. C., ZHAO, K., CHANG, L., YIN, G. P., ZHAO, H. J., LIU, S. Q. & TANG, Z. Y. 2014. Carbonized Nanoscale Metal-Organic Frameworks as High Performance Electrocatalyst for Oxygen Reduction Reaction. *Acs Nano,* 8**,** 12660-12668.